
Material optimization: Magnetic thin films and advanced Spintronic devices

Rafael Girão (72916)¹

¹*Engineering Physics*

(Dated: December, 2017)

One of the current state-of-the-art options in magnetic sensing field applications is the magnetoresistive effect based on MgO magnetic tunnel junctions (MTJs). The junctions were deposited in a magnetron sputtering system with $\sim 8\%$ Non-uniformity values. An optimization of the materials used was performed in order to obtain MTJs with linear response, using either shape anisotropy, permanent magnets or superparamagnetic like behaviour, reaching sensitivity values of $\sim 40\% \text{ mT}^{-1}$, $\sim 6 - 18\% \text{ mT}^{-1}$ and $\sim 13\% \text{ mT}^{-1}$, respectively

I. Introduction

A. Magnetic sensors

Spintronic devices based on the magnetoresistive (MR) effect have been widely used and explored over the past years especially in the magnetic recording industry. Several techniques for magnetic field sensing exist, operating on different physical phenomena with each having a specific application. There are Hall effect sensors, based on the Lorentz force acting on the moving electrons, mostly used for mechanical applications as proximity sensors. SQUIDs, based on Josephson junctions, which require operation at very low temperature, have very high detectivity values (fT - nT range) and are mostly used on biological applications. Inductor sensors based on the electromotive force generated in a coil, can work in the pT - mT range. Flux-gates, using a ferromagnetic core surrounded by a drive and a sensing coil, mostly used in military applications work in the nT - mT range. Nuclear magnetic resonance, based on the nuclear precession of atomic spin when in the presence of an external field, operates with very high sensitivity at the nT range, and is used for medical applications [1, 2].

MR sensors come as an additional type of magnetic field sensors that are based on the MR effect of magnetic thin film layers. Mostly used for the magnetic recording industry, they can be adapted to other applications, which benefit from their high performance, lower power consumption, small footprint and lower fabrication costs. There are several types of MR effects: anisotropic magnetoresistance (AMR), giant magnetoresistance (GMR) and tunnelling magnetoresistance (TMR).

An MR sensor resistance varies with an applied magnetic field. This change is known as the magnetoresistance of the device, and is defined by:

$$\text{MR} = \frac{R_{max} - R_{min}}{R_{min}} \times 100 \quad (\%) \quad (1)$$

Typical MR values for AMR and GMR based sensors are 2% - 6% and 6% - 20% respectively. The TMR effect

can be further divided in two: Tunnelling in an amorphous insulating material (incoherent tunnelling), typically AlO_x , or tunnelling through a crystalline insulating material (coherent tunnelling), typically MgO. For AlO_x MR sensors, values on the order of $\sim 70\%$ are usually obtained, while for MgO values can go as high as $\sim 300\%$ [3, 4].

B. Magnetic tunnel junctions

The sensors used in this work were MgO based. The working principle is the spin-dependent tunnelling (SDT) effect of electrons crossing an insulator (I), between two ferromagnetic electrodes (FM), forming a tunnel junction. For a sufficiently small insulating barrier, when a bias voltage is applied, electrons will tunnel through. The barrier must be thin enough to allow tunnelling and big enough to stop the roughness of the FM films from creating pinholes in the barrier. The conductance will be affected by the relative magnetization states of both electrodes. The first model for the TMR effect was proposed by Julliere (1975) [5] in which the tunnelling conductance through the barrier depends only on the density of states at the Fermi level of each FM electrode. He obtained 14% MR values in Fe/Ge/Co junctions at 4.2 K. Later, Moodera [6] introduced a junction based on Al_2O_3 with TMR values over 10% at room temperature. Finally, in 2004, Parkin [8] and Yuasa [7] simultaneously introduced MgO based tunnel junctions, with TMRs of 220% based on Fe/MgO/Fe junctions, which were quickly after introduced to the magnetic memory industry [9].

Tunnelling through an MgO barrier differs from AlO_x as the MgO barrier is itself crystalline, with a bcc (001) structure. If the crystalline structure of the FM electrodes can match that of the MgO, the crystalline symmetry throughout the barrier will allow different Bloch states to tunnel with different probabilities [10]. The Δ_1 Bloch states have the higher tunnelling probability along with the higher spin polarization. MgO based magnetic tunnel junctions (MTJ) present a much higher TMR value, due to this effect which can be regarded as

a symmetry filtering effect, and coherent tunnelling.

To work as a sensor MTJs have one of the ferromagnetic electrodes magnetically pinned (pinned layer, PL) while the other is left free to rotate with external magnetic fields (free layer, FL). $\text{Co}_{40}\text{Fe}_{40}\text{B}_{20}$ is used for both FM electrodes. Being amorphous in the as deposited state, it doesn't influence the growth of the MgO (001) structure. When annealed, Boron diffusion changes the composition of the FM electrodes, which quickly crystallize taking the MgO (001) structures as template. This way, the use of CoFeB allows for a simple and effective way of obtaining low lattice mismatch between electrodes and barrier allowing the coherent tunnelling effect to occur [11–13]. The pinning can be performed through the use of a synthetic anti ferromagnetic structure (SAF), composed of two ferromagnetic layers, separated by a thin conductive layer, typically of Ru. Coupling between the ferromagnetic layers is achieved through a RKKY-type interaction. One of the ferromagnetic layers is pinned to an antiferromagnetic layer through exchange bias. $\text{Mn}_{62}\text{Pt}_{38}$ was used as the antiferromagnet, coupled to a $\text{Co}_{70}\text{Fe}_{30}$ layer. The CoFe layer is separated from the pinned layer in the FM/I/FM sandwich by a Ru layer with approximately ~ 0.75 nm.

C. MTJs as sensors

When working as a sensor, the voltage output measured across the junction can be approximated as:

$$\Delta V = \frac{1}{2} \frac{\text{TMR} I \text{RA}}{w h} \cos(\theta), \quad (2)$$

where θ is the angle between magnetization directions, RA is the resistance area product of the junction, which is constant for a given MgO thickness, w and h are respectively the width and height of the pillar geometry, I is the bias current and TMR is the MR value of the junction [4].

With one of the FM layers pinned, the response of the sensor will depend on the behaviour of the free layer. To work as a sensor, the free layer must be manipulated in order to control its magnetic hysteresis. When an external field is applied perpendicularly to the magnetization, a coherent rotation process can be assumed to take place, which allows the approximation of the free layer as mono-domain like, with all magnetic moments in the FL aligned and rotating as one. This type of behaviour can be described by the Stoner-Wohlfarth model, in which the direction of the magnetization, is calculated by the energy minima on the FL, assuming uniform magnetization.

The energy in the free layer can be described as:

$$E_{fl} = -\mu_o M_s (H_{ext} - H_{off}) \cos \theta + \frac{\mu_o}{2} M_s H_k \sin^2 \theta + \frac{\mu_o}{2} N_h M_s^2 \cos^2 \theta' \quad (3)$$

where the first term in the right hand side of the equation is the Zeeman term from the external field (H_{ext}), the SAF and the Neel coupling ($H_{off} = H_{SAF} - H_N$). The second term is the induced uni-axial anisotropy obtained from magnetic annealing and deposition of the ferromagnetic film with applied magnetic field. The energy associated with the FL has two types of contributions: internal anisotropy sources and external applied fields. The internal anisotropies are the induced uni-axial anisotropy, from magnetic annealing and deposition under a magnetic field, and the shape anisotropy which creates the demagnetizing field inside the FL. The induced uni-axial anisotropy will force the magnetization to align with an easy axis direction, and can be expressed in terms of an H_k field, corresponding to the magnetic field necessary to overcome its effect. The last term is the term due to shape anisotropy, where N_h is the demagnetizing tensor. This term will force the magnetization to align in the larger dimension of the junction geometry, to minimize the demagnetizing field inside the free layer. M_s is the magnetization of the free layer and θ is the angle of the magnetization with the easy axis direction defined as the easy direction from the induced uni-axial anisotropy, which is the same for both the FL and PL.

Minimization of the energy results in a condition for no coercivity given by:

$$H_k < N_h M_s \quad \text{and} \quad \cos(\theta) = \frac{H_{ext} - H_{off}}{N_h M_s - H_k}, \quad (4)$$

External fields contribute with a Zeeman energy term to the FL energy. Neel coupling is due to roughness in the FM interfaces, while the SAF contribution comes from its stray field.

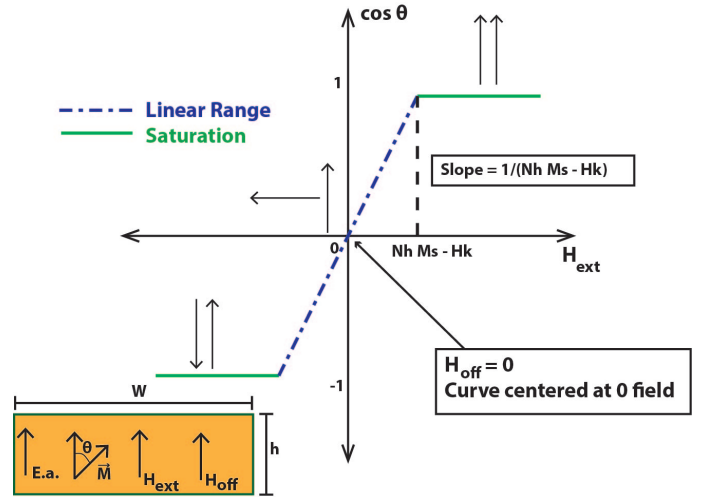


Figure 1: Orientation of the magnetization with an applied magnetic field in the PL easy axis direction. Linear transfer curve is obtained when the shape anisotropy energy is higher than the induced uni-axial anisotropy.

Having perpendicular easy axis from the induced anisotropy term, can be achieved by a two step deposi-

tion process, and results in a hysteresis free response at all times, although such process was not analysed during the work.

The linearization condition can also be achieved by applying an external field in the longitudinal direction of the free layer, acting in the same direction as the shape anisotropy. This external field can be created by adding a permanent magnet near the MTJ which will influence the free layer behaviour [15, 16]. The magnet adds a Zeeman term in the direction perpendicular to the free layer easy axis:

$$E_{PM} = -\mu_0 M_s H_{PM} \sin(\theta), \quad (5)$$

and the condition for linearity near zero applied field is given by:

$$H_k < N_h M_s + H_{pm}, \quad (H_{pm} : \text{Perm. magnet}) \quad (6)$$

where H_{PM} is the field created by the permanent magnet.

Another strategy to promote hysteresis free MR curves is to reduce the thickness of the FL down to a critical size, where after annealing, the film will become granular with superparamagnetic-like structures [17, 18]. The magnetization of these particles oscillates rapidly due to thermal excitations, in a Brownian type motion, even though all magnetic moments are still aligned, as in a ferromagnet. The magnetization can still be aligned to an external field, as it will average over a particular value and will present no coercivity. Its behaviour can be modelled under the framework of Langevin's theory of superparamagnetism:

$$M(H) \approx n \mu L\left(\frac{\mu_0 \mu H}{k_B T}\right), \quad L(x) = \frac{1}{\tanh(x)} \frac{1}{x}, \quad (7)$$

where μ is the magnetic moment of the particles and n the number of particles.

II. Material characterization

The stack used for the MTJ sensor fabrication was Ta 5 / [Ru 18 / Ta 3] x 3 / Mn₆₂Pt₃₈ 20 / Co₇₀Fe₃₀ 2.2 / Ru 0.75 / Co₄₀Fe₄₀B₂₀ 3 / MgO t1 / Co₄₀Fe₄₀B₂₀ t2 / Ru 10 / Ta 5 (nm). MgO and Co₄₀Fe₄₀B₂₀ free layer thickness was varied.

MTJ samples were deposited in a Nordiko 2000 magnetron sputtering system. Test samples were prepared to control deposition rate of the system, and to perform VSM measurements. The magnetization and H_k of the ferromagnetic films was obtained from an hard axis VSM measurement. Results for the deposition rate and magnetic properties are presented in table (I).

Thickness uniformity of the magnetic materials deposited in a 2 inch² sample was assessed and compared for the cases of a deposition with applied field and a deposition without applied field for easy axis definition, with the results shown in figure 2. With an applied field, a

Target Material	Deposition rate (Å/s)	$\mu_0 H_k$ (mT)	M_s (kA/m)
MnPt	1.2 ± 0.05	-	-
Ru	0.7 ± 0.01	-	-
Ta	0.65 ± 0.01	-	-
CoFeB	0.35 ± 0.04	2.30	1140
MgO	0.095 ± 0.004	-	-
CoFe	0.42 ± 0.03	24.2	1896

Table I: Nordiko 2000 materials deposition rates and magnetic properties, in a deposition with applied magnetic field for easy axis definition.

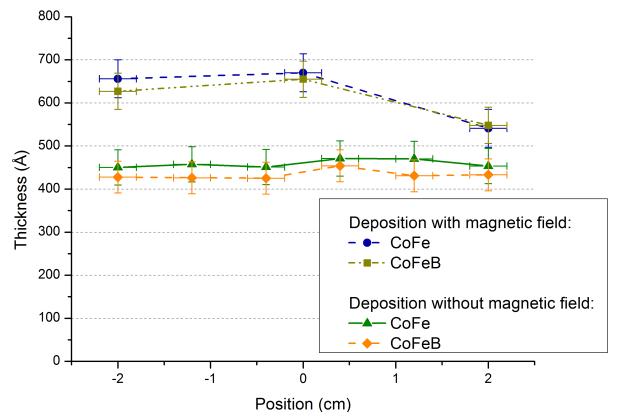


Figure 2: Measurements in the easy axis direction of a 2 inch² sample, for both magnetic materials. Results shown for a deposition with and without applied magnetic field. Samples without magnetic field were deposited for 1000s, while CoFe and CoFeB with magnetic field were deposited for 1600s and 1800s respectively.

variation from the middle to the bottom of the sample of 19.24% was measured for CoFe, and 17.83% for CoFeB, in the direction of the field. This can represent significant changes in sensor performance over the sample which can damage sensor yield for a batch of samples. The results without magnetic field, resulted in no change throughout the sample (only variations covered by the measurement error), suggesting that the applied field in the deposition influences the uniformity of the material deposited.

In figure 3 a VSM measurement of the full MTJ stack is presented, for a CoFeB free layer thickness of 3 nm. The values of $\mu_0 H_{exch} \approx 90$ mT and $\mu_0 H_{Neel} \approx -0.2916$ mT were obtained, where the Neel field was calculated from the offset from zero of the curve, since for unpatterned samples the SAFs stray field will not contribute with a magnetostatic field.

Electrical characterization of several samples with increasing MgO thickness demonstrated that the MTJs RA product increases exponentially as the barrier thickness

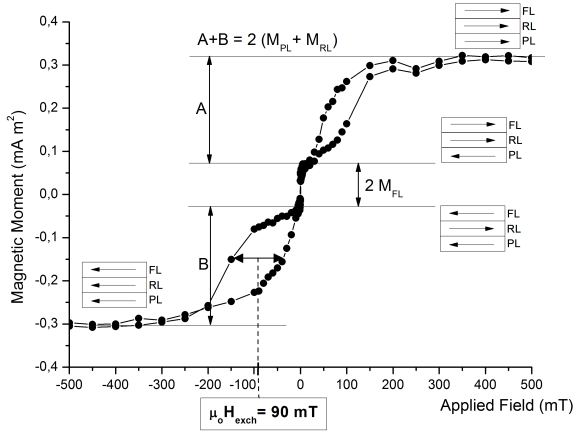


Figure 3: VSM measurement of the full MTJ stack, with a CoFeB free layer of 3 nm, and after magnetic annealing at 330°C for 2 hours at 0.5T applied field.

is increased. The samples RA value was considered to be the centre of the RA distribution, calculated through a gaussian fit. Figure 4 shows the increase in RA with MgO thickness. From equation (2), the resistance of the junction can be seen to directly increase the measured output. Increasing the MgO barrier also results in an increased robustness of the sensors, as it can withstand higher voltages before having its MR dropped by half or until breakdown. With an MgO thickness of 1.05 nm, the voltage required for the TMR to drop by half was $\sim 0.194\text{V}$, with a breakdown of the junction achieved at 0.902V . Increasing the MgO to 2.0 nm resulted on an approximate voltage of $\sim 0.505\text{V}$ for half the MR to be lost, and 2.3V to reach a breakdown.

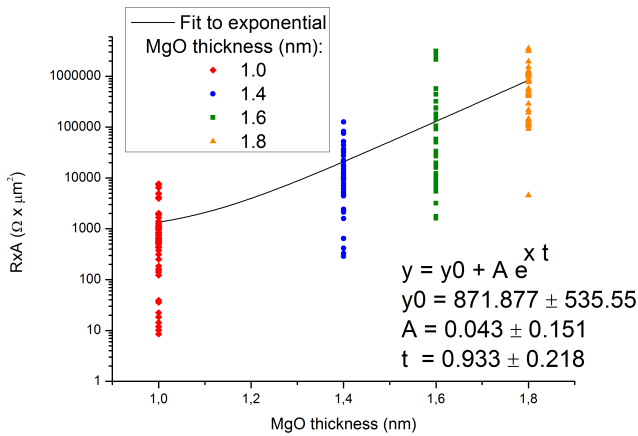


Figure 4: Exponential increase in RA. The RA axis is in logarithmic scale, and the black line is a fit to the central values of the RA distribution. The tail of data points that drags below the curve is a result of shorting in the fabricated MTJs.

Because the magnetic field applied during deposition seems to affect the distribution of thickness, two samples of 2inch^2 size, were deposited and fabricated, with and without applied magnetic field. The sample deposited with magnetic field presented RA around $\sim 88.25\%$ of the value obtained without magnetic field, with similar distribution, suggesting that MgO deposition is also affected by the presence of this field, which may interact with the plasma in the magnetron sputtering system. Defining Non-uniformity as:

$$NU = \frac{MR_{\max} - MR_{\min}}{MR_{\max} + MR_{\min}} \times 100 \quad (\%), \quad (8)$$

deposition with magnetic field in the magnetron sputtering system used, has a Non-uniformity of $\pm 22.8\%$ over the 2inch^2 sample, while deposition without magnetic field has 8.33%. When looking only at an area of 1inch^2 , similar uniformities were obtained for both, with deposition with magnetic field having a Non-uniformity of $\pm 7.89\%$. This sample displayed a decrease in the MR values near the bottom area of the sample, in the easy axis direction, similar to the thickness distribution case, which was not verified for the deposition without magnetic field.

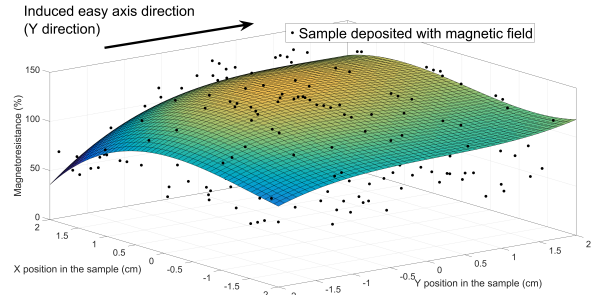


Figure 5: Distribution of the MR values of junctions deposited in the magnetron sputtering system with an applied magnetic field to induce an easy axis. A decrease on the MR values is observed near the negative Y position similar to the decrease observed previously for the thickness distribution.

III. Linearization of the sensor

Linearization of the transfer curve of the MTJ sensor was performed either by varying the shape anisotropy, by permanent magnet integration or by employing a superparamagnetic-like free layer.

Shape anisotropy

Shape anisotropy influences the linearity of the sensor by providing a direction in which the demagnetizing

field is very strong, and a dimension where it is smaller, forcing the magnetization to align in the direction with smaller energy, and thus providing a longitudinal bias of the sensor. An approximation for the demagnetizing field at the center of the free layer is given by:

$$\begin{aligned} H_d^h &= \frac{8 M_s}{4 \pi} \frac{w}{h \sqrt{w^2 + h^2}} t \cos(\theta) \\ H_d^w &= \frac{8 M_s}{4 \pi} \frac{h}{w \sqrt{w^2 + h^2}} t \sin(\theta) \end{aligned}, \quad (9)$$

where H_d^h and H_d^w are the demagnetizing field in the h and w direction, respectively, with θ the angle of the magnetization with the easy axis [3].

With samples fabricated with a CoFeB FL with 1.55 (nm) and 1.8 (nm) thickness several samples were evaluated regarding their coercivity and sensitivity values with average measurements presented in figure 6. Sensitivity and coercivity tend to decrease with increased shape ratio w/h , although when $w \gg h$ a change of width no longer affects coercivity. On the other hand variation of the h dimension is still effective, with smaller values providing lower coercivities. Dimensions of $1 \mu\text{m}$ for this dimension were experimented, but resulted in a large number of non working sensors, which suggest the current microfabrication process is not suitable for junctions of this size.

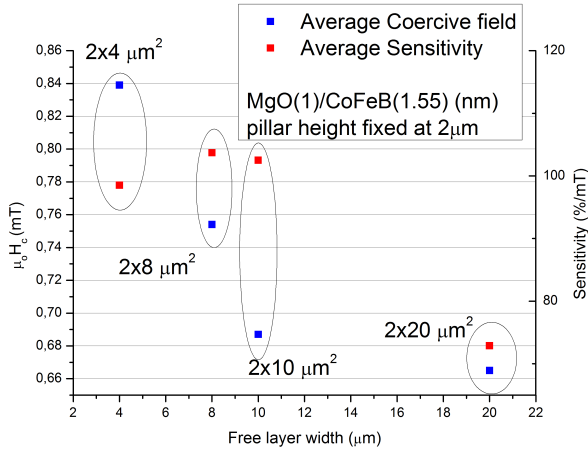


Figure 6: Single sensor coercivity and sensitivity with fixed height where coercivity is seen to decrease. Measurements performed on samples with 15 junctions of each size.

Variation of the CoFeB free layer thickness for a constant shape of $2 \times 20 \mu\text{m}^2$ results in a decrease of the TMR value of the MTJ, although it improves both coercivity values and linear operating range, with a decrease in sensitivity (figure 7). This variation is useful as it improves the MTJ behaviour from a sensing application point of view. CoFeB thickness in the range 1.5 - 1.55 nm were used for most of the fabricated sensors.

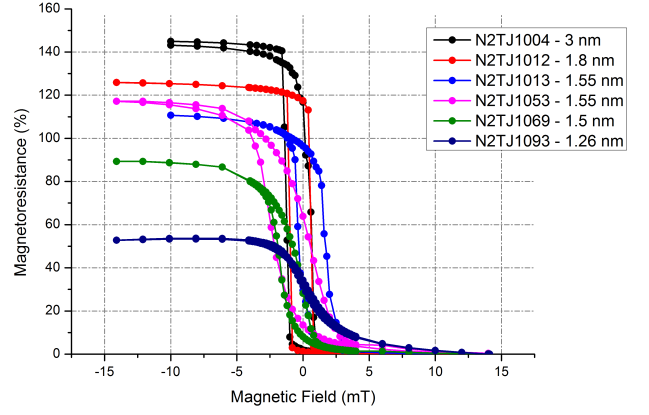


Figure 7: Evolution of the sensor transfer curve by varying the CoFeB free layer thickness for a fixed rectangular shape of $2 \times 20 \mu\text{m}^2$.

Integration in array configuration of sensors biased with shape anisotropy only

Adding single tunnel junctions in series will improve the sensitivity of the device in terms of measured voltage per mT, as the resistance will be increased by the amount of junctions fabricated in series. Although the same MR is expected in both single and series MTJs, the latter usually presents lower MR values, which can be attributed partially to the shorting of some junctions during the etching steps. Figure 8 shows a comparison between a single MTJ transfer curve, and an array of 24 MTJs. Although similar sensitivity values are obtained for the relative change in resistance (due to similar MR values) the sensitivity in ΩmT^{-1} , converted directly into $\text{mV mA}^{-1} \text{mT}^{-1}$, is much higher for the array configuration.

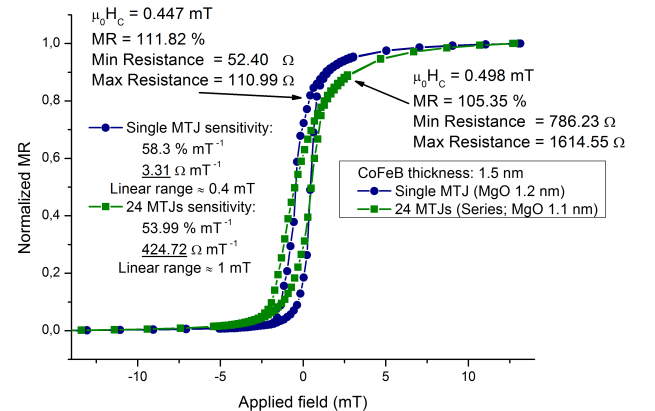


Figure 8: Transfer curve comparison of and array of 24 MTJs assembled in series, compared with a single MTJ.

These samples were micro fabricated in a Wheatstone bridge configuration (figure 9), for industrial application, where each branch was required to be balanced up to a critical voltage of 250 mV when biased at 5V.

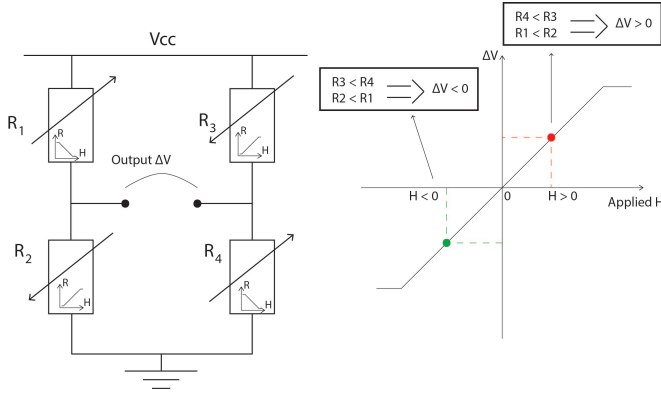


Figure 9: Configuration of a Wheatstone bridge. The resistances correspond to MTJ sensing devices, represented as a varying resistance.

Several samples were fabricated, with different MgO thickness, and CoFeB \sim 15 nm. The yield of the process is given by the ratio of balanced Wheatstone bridges (one for each chip) to total amount of bridges in the sample, and defined as:

$$yield = \frac{N_{balanced\ chips}}{N_{total\ chips}} \quad (\%). \quad (10)$$

A maximum yield value of 71 % is achieved for a MgO thickness of 1.2 nm, with the yield value seen to increase for lower thickness. This was attributed to the fact that a balanced Wheatstone bridge requires balanced resistance, which increases exponentially with the thickness of the MgO layer, provided that the shape is maintained. Therefore the same variation in thickness, due to non perfect uniformity of the micro fabrication process, will result in an increasingly higher resistance variation for higher MgO thickness. In figure 10 a graphic of the RA distribution versus MR is shown for the samples processed, where the standard deviation to mean value ratio of all samples, except the ones with micro fabrication problems, was smaller or on the order of the uniformity of the magnetron sputtering machine (\sim 8 %).

Permanent Magnet Linearization

Integration of permanent magnets was performed for sensor geometries of $2 \times 20 \mu\text{m}^2$, $4 \times 20 \mu\text{m}^2$, $2 \times 10 \mu\text{m}^2$ and a circular shape of $3.5 \mu\text{m}$ radius, which was chosen to obtain the same RA value as the 2×20 shape. A range of permanent magnets was fabricated in a top magnet and side magnet configuration, where the permanent magnet is placed on top of the pillar, and on the sides of

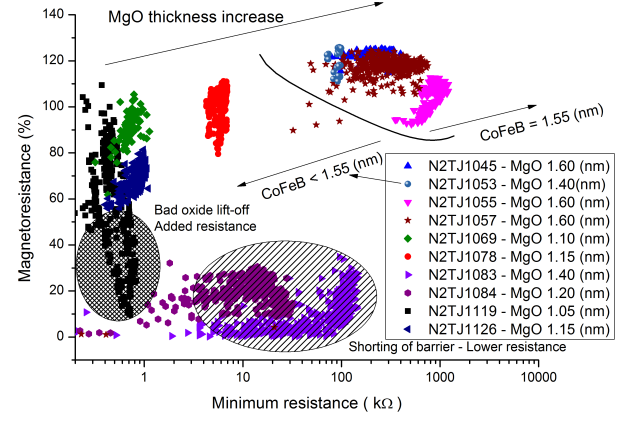


Figure 10: RA versus MR distribution of the samples fabricated in an array configuration. The spread in the black data from sample N2TJ1119 is due to resistance being added in series to the pillar, which can be explained by a bad oxide lift off of passivation layers. Samples N2TJ1083 and N2TJ1084 show a spread in the other direction, with decreasing resistance from added parallel metallic conduction in the barrier, providing an alternative to the tunnelling effect, and disrupting the MR response

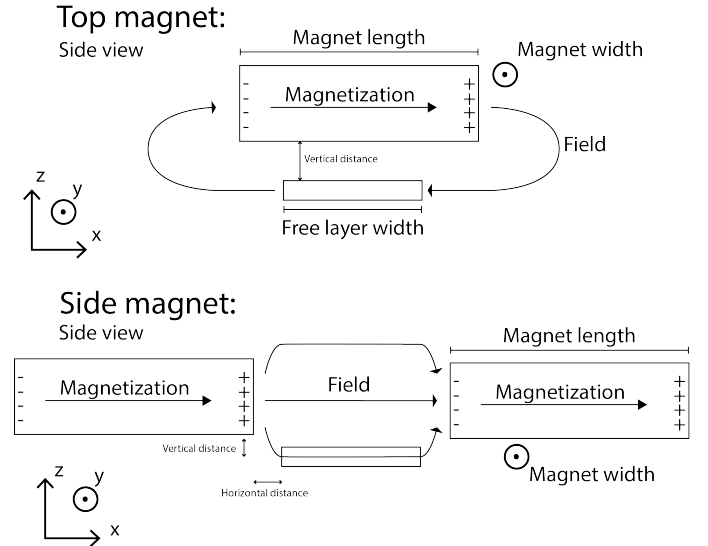


Figure 11: Side view illustration of both permanent magnet configurations used.

the pillar respectively (figure 11). In both cases a magnetic field perpendicular to the PL easy axis is obtained providing a longitudinal bias to the free layer.

Numerical calculation for the magnetic field generated by the permanent magnets is performed through the expression:

$$\vec{H}(\vec{r}) = \int_V \frac{\nabla \cdot \vec{M}}{|\vec{r} - \vec{r}'|^3} (\vec{r} - \vec{r}') d^3 r' + \int_S \frac{\vec{n} \cdot \vec{M}}{|\vec{r}' - \vec{r}|} (\vec{r}' - \vec{r}) d^2 r'. \quad (11)$$

This field was averaged over the size of the free layer. The values of H_k were taken from the VSM measurements and H_d (demagnetizing field) approximated by equation (9). Permanent magnets used on sensors were fabricated with dimensions of $[2\ \mu\text{m}\ 12\ \mu\text{m}\ 24\ \mu\text{m}\ 36\ \mu\text{m}\ 48\ \mu\text{m}\ 60\ \mu\text{m}]$ in both dimensions, creating matrices of 6×6 values, used to probe the effect of permanent magnet dimensions on the sensor behaviour.

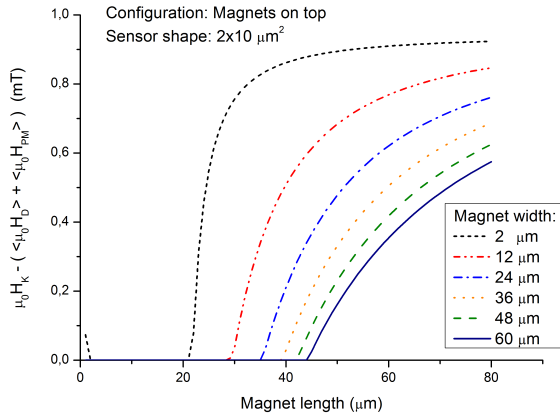


Figure 12: Top magnet configuration. Numerical calculation of coercivity with increased length and width of PM integrated for device linearization.

For the side magnet configuration the magnetic field created at the free layer of the sensor increases with magnet size in either dimension, as both dimensions will increase the magnetic moment of the permanent magnets. The same doesn't happen for the top magnet configuration, where the maximum field at the free layer is obtained for magnet lengths on the order of the sensor width. While increasing the width of the magnet increases the magnetic field by increasing the magnetic moment, in the case of the length, the magnetic dipoles are placed further away from the sensor as the dimension increases, which has stronger effect than the increase in magnetic moment. Thus magnetic field is highest for a magnet length close the sensor width in the top magnet configuration, while the remaining dimension increases it up to a limit. The effect on the coercivity is inverted, with lower coercivity values obtained for magnet lengths close to sensor width (top magnets), and for the highest magnet size (side magnets).

In both cases the qualitative behaviour of the coercivity with magnet shape is predicted by the numerical calculations. The difference between the real values, obtained experimentally, and the calculated values can be explained by the simplicity of the model used, which assumes perfect geometries and simplistic behaviour of the magnetization inside the free layer, in which a macrospin approximation was considered. The sample were fabricated with 3 nm of CoFeB free layer thickness, but ob-

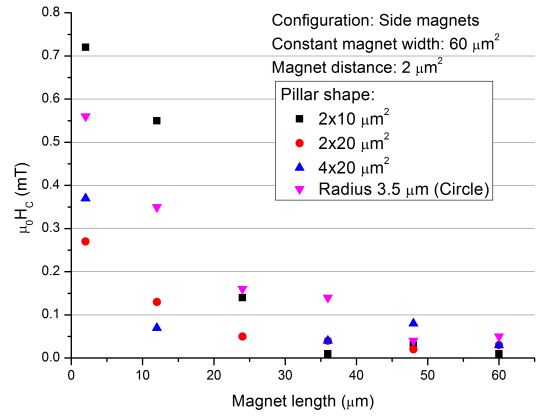


Figure 13: Side magnet configuration. Coercivity as a function of the magnet length for the various sensor shapes utilized.

tained MR values of only $\sim 80\%$, damaging the sensitivity of the device. A transfer curve without coercivity was obtained for all shapes. Sensors with shape $4 \times 20\ \mu\text{m}^2$ and $3.5\ \mu\text{m}$ were harder to linearize, only achieving close to zero coercivity at the very limit in the top magnet configuration. Higher sensitivities were obtained for the magnet on side configuration ($\sim 18\ \text{mT}^{-1}$) than for the magnet on top ($\sim 6\ \text{mT}^{-1}$).

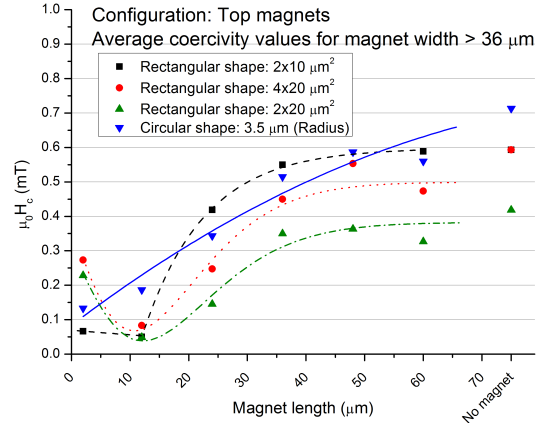


Figure 14: Top magnet configuration. Coercivity as a function of the magnet width for the various sensor shapes utilized.

In figure 15 a comparison between two representative curves obtained for a sensor shape of $2 \times 10\ \mu\text{m}^2$ is shown, where a much higher linear operating range is obtained for the top magnet integration, although having lower sensitivity values. Both strategies can achieve device linearization. If lower footprint is required, Top magnet integration seems the best alternative, as it occupies less area, while if loss of sensitivity is an issue, than side mag-

nets should be considered.

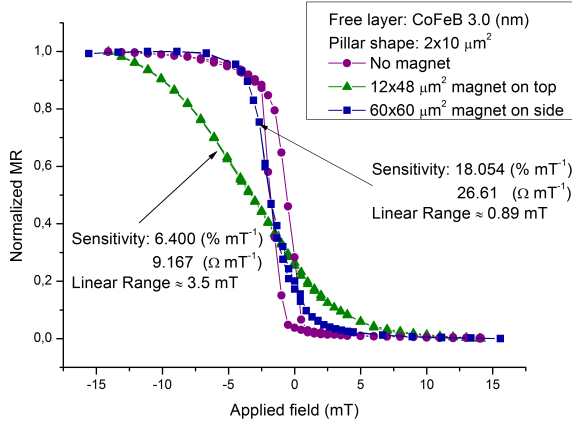


Figure 15: Comparison between representative curves obtained for a sensor shape of $2 \times 10 \mu\text{m}^2$ with permanent integration. The transfer curve of a sensor with the same shape but without permanent magnet is shown as well for comparison.

Superparamagnetic-like behaviour

Only two of the fabricated samples displayed superparamagnetic-like behaviour. One, by decreasing the samples free layer thickness below 1.3 nm (Sample [1]), and the other by performing an annealing at a higher temperature than usual in a 1.5 nm thick free layer (375°C for 2 hours, Sample [2]). Both samples presented an hysteresis free transfer curve although with very small MR, especially in the case of sample [2]. By fitting the transfer curves to equation (9), the volume of the superparamagnetic particles was $1.4 \times 10^{-18} \text{ cm}^3$, for sample [2], and $3.6 \times 10^{-18} \text{ cm}^3$. The sample with higher free layer thickness having higher particle volume is in accordance to other works [17, 18]. Representative transfer curves for both samples are shown in figure 16.

IV. Conclusion

Magnetoresistive sensors with linear response were obtained by manipulating the junctions shape, although presenting residual coercivity ($\sim 0.4 \text{ mT}$), and sensitivities of $\sim 40\% \text{ mT}^{-1}$, varying between $0.2 \text{ k}\Omega \text{ mT}^{-1}$ and $349.85 \text{ k}\Omega \text{ mT}^{-1}$.

Junctions were built into Wheatstone bridges and integrated in chips for industrial application in processes with maximum yields of 71% for a sample with 1.2 nm thick MgO barrier. Balanced chip yield was higher for lower MgO thickness, and thus lower resistance devices. Sensor shape can be changed to address the issue, as well

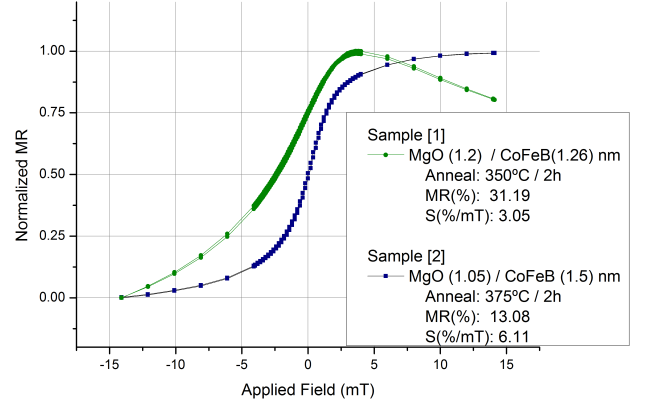


Figure 16: Representative transfer curve for the two samples fabricated with superparamagnetic-like behaviour.

as the increase of the number of junctions in series, although for the former the curve of the sensor would be different and less linear, while for the latter it would result in an increased footprint.

Two extra strategies were used to linearize the junctions free layer. By using permanent magnets in two configurations (Side and Top of the junction), with hysteresis free curves obtained for both and sensitivities of $\sim 6\% \text{ mT}^{-1}$ and $13\% \text{ mT}^{-1}$. By achieving superparamagnetism in the free layer sensitivities of $\sim 13\% \text{ mT}^{-1}$ were obtained with hysteresis free curves as well.

-
- [1] S. Tumanski *Przegląd elektrotechniczny* R. 89, 2013
- [2] J. Lenz, S. Edelstein *Magnetic sensors and their applications* IEEE Sensors Journal, 6(3): 631-649, June 2006. ISSN 1530-437X.
- [3] Silva, Ana V., Leitao, Diana C., Valadeiro, João, Amaral, José, Freitas, Paulo P., and Cardoso, Susana. *Linearization strategies for high sensitivity magnetoresistive sensors* Eur. Phys. J. Appl. Phys., 72(1):10601, 2015.
- [4] P. P. Freitas, R. Ferreira, and S. Cardoso *Spintronic sensors* Proceedings of the IEEE, 104(10): 1894–1918, Oct 2016. ISSN 0018-9219
- [5] M. Julliere *Tunneling between ferromagnetic films* Physics Letters A, 54(3):225 – 226, 1975. ISSN 0375-9601.
- [6] J. S. Moodera, L. R. Kinder, T. M. Wong, and R. Meservey *Large magnetoresistance at room temperature in ferromagnetic thin film tunnel junctions* Phys. Rev. Lett., 74:3273–3276, Apr 1995. doi: 10.1103/PhysRevLett.74.3273.
- [7] S. Yuasa, T. Nagahama, A. Fukushima, Y. Suzuki, and K. Ando. *Giant room-temperature magnetoresistance in single-crystal fe/mgo/fe magnetic tunnel junctions*. Nature Materials, 3(12):868–871, 2004
- [8] S. Parkin, C. Kraiser, B. Hughes, M. Samant, S. Yang, A. Panchula, and P. Rice *Giant tunnelling magnetoresistance at room temperature with mgo (100) tunnel barriers*. Nature Materials, 3(12):862–867, 2004.
- [9] Koji Tsunekawa, David D. Djayaprawira, Motonobu Nagai, Hiroki Maehara, Shinji Yamagata, Naoki Watanabe, Shinji Yuasa, Yoshishige Suzuki, and Koji Ando *Giant tunneling magnetoresistance effect in low-resistance magnetic tunnel junctions for read-head applications* Appl. Phys. Lett. 87, 072503 (2005)
- [10] W. H. Butler *Tunneling magnetoresistance from a symmetry filtering effect* Science and Technology of Advanced Materials, 9(1):014106, 2008.
- [11] Y. M. Lee, J. Hayakawa, S. Ikeda, F. Matsukura, and H. Ohno *Effect of electrode composition on the tunnel magnetoresistance of pseudo-spin-valve magnetic tunnel junction with a MgO tunnel barrier* Appl. Phys. Lett. 90, 212507 (2007);
- [12] S. Ikeda, J. Hayakawa, Y. M. Lee, T. Tanikawa, and F. Matsukura and H. Ohno *Tunnel magnetoresistance in MgO-barrier magnetic tunnel junctions with bcc-CoFe₂B... and fcc-CoFe free layers* JOURNAL OF APPLIED PHYSICS 99, 08A907 2006
- [13] Sumanta Mukherjee et al *Role of boron diffusion in CoFeB/MgO magnetic tunnel junctions* PHYSICAL REVIEW B 91, 085311 (2015)
- [14] P. P. Freitas, R. Ferreira, S. Cardoso, and F. Cardoso *Magnetoresistive sensors* Journal of Physics: Condensed Matter, 19(16):165221, 2007
- [15] R. C. Chaves, S. Cardoso, R. Ferreira, and P. P. Freitas *Low aspect ratio micron size tunnel magnetoresistance sensors with permanent magnet biasing integrated in the top lead* Journal of Applied Physics 109, 07E506 (2011)
- [16] Ricardo J. Janeiro , Luís Gameiro , António Lopes , Susana Cardoso , Ricardo Ferreira , Elvira Paz , and Paulo P. Freitas *Linearization and Field Detectivity in Magnetic Tunnel Junction Sensors Connected in Series Incorporating 16 nm-Thick NiFe Free Layers* IEEE TRANSACTIONS ON MAGNETICS, VOL. 48, NO. 11, NOVEMBER 2012
- [17] Jiangwei Caoa, Yan Liuc, Yang Rena, Fulin Weia, P.P. Freitas *Effect of annealing temperature on formation of superparamagnetism in CoFeB/MgO/CoFeB magnetic tunnel junctions* Applied Surface Science 314 (2014) 443–446
- [18] Weifeng Shen, Benaiah D. Schrag, Anuj Girdhar, Matthew J. Carter, Hai Sang, and Gang Xiao *Effects of superparamagnetism in MgO based magnetic tunnel junctions* PHYSICAL REVIEW B 79, 014418 2009